

# Rogue Waves and Large Deviations in Deep Sea

Giovanni Dematteis,<sup>1,2</sup> Tobias Grafke,<sup>3</sup> and Eric Vanden-Eijnden<sup>1</sup>

<sup>1</sup>*Courant Institute, New York University, 251 Mercer Street, New York, NY 10012, USA*

<sup>2</sup>*Dipartimento di Scienze Matematiche, Politecnico di Torino,  
Corso Duca degli Abruzzi 24, I-10129 Torino, Italy*

<sup>3</sup>*Mathematics Institute, University of Warwick, Coventry CV4 7AL, United Kingdom*

(Dated: January 24, 2018)

The appearance of rogue waves in deep sea is investigated using the modified nonlinear Schrödinger (MNLS) equation in one spatial-dimension with random initial conditions that are assumed to be normally distributed, with a spectrum approximating realistic conditions of a uni-directional sea state. It is shown that one can use the incomplete information contained in this spectrum as prior and supplement this information with the MNLS dynamics to reliably estimate the probability distribution of the sea surface elevation far in the tail at later times. Our results indicate that rogue waves occur when the system hits unlikely pockets of wave configurations that trigger large disturbances of the surface height. The rogue wave precursors in these pockets are wave patterns of regular height but with a very specific shape that is identified explicitly, thereby allowing for early detection. The method proposed here combines Monte Carlo sampling with tools from large deviations theory that reduce the calculation of the most likely rogue wave precursors to an optimization problem that can be solved efficiently. This approach is transferable to other problems in which the system's governing equations contain random initial conditions and/or parameters.

Rogue waves, long considered a figment of sailor's imagination, are now recognized to be a real, and serious, threat for boats and naval structures [1, 2]. Oceanographers define them as deep water waves whose crest-to-trough height  $H$  exceeds twice the significant wave height  $H_s$ , which itself is four times the standard deviation of the ocean surface elevation. Rogue waves appear suddenly and unpredictably, and can lead to water walls with vertical size on the order of 20–30 m [3, 4], with enormous destructive power. Although rare, they tend to occur more frequently than predicted by linear Gaussian theory [5, 6]. While the mechanisms underlying their appearance remain under debate [7–9], one plausible scenario has emerged over the years: it involves the phenomenon of modulational instability [10, 11], a nonlinear amplification mechanism by which many weakly interacting waves of regular size can create a much larger one. Such an instability arises in the context of the focusing nonlinear Schrödinger (NLS) equation [11–17] or its higher order variants [18–22], which are known to be good models for the evolution of a unidirectional, narrow-banded surface wave field in a deep sea. Support for the description of rogue waves through such envelope equations recently came from experiments in water tanks [23–26], where Dysthe's MNLS equation in one spatial dimension [18, 19] was shown to accurately describe the mechanism creating coherent structures which soak up energy from its surroundings. While these experiments and other theoretical works [27, 28] give grounds for the use of MNLS to describe rogue waves, they have not addressed the question of their likelihood of appearance. Some progress in this direction has been recently made in [29], where a reduced model based on MNLS was used to estimate the probability of a given amplitude within a certain time, and thereby compute the tail of the surface height distribution. These calculations were done using an ansatz for the solutions of MNLS, effectively making the problem two-dimensional. The purpose of this paper is to remove this approximation, and study the problem in its full generality. Specifically, we consider the MNLS with random initial data drawn from a Gaussian distribution [30]. The spectrum of this field is chosen to have a width comparable to that of the JONSWAP spectrum [31, 32] obtained from observations in the North Sea. We calculate the probability of occurrence of a large amplitude solution of MNLS out of these random initial data, and thereby also estimate the tail of the surface height distribution. These calculations are performed within the framework of large deviations theory (LDT), which predicts the most likely way by which large disturbances arise and therefore also explains the mechanism of rogue wave creation. Our results are validated by comparison with brute-force Monte-Carlo simulations, which indicate that rogue waves in MNLS are indeed within the realm of LDT. Our approach therefore gives an efficient way to assess the probability of large waves and their mechanism of creation.

## I. PROBLEM SETUP

Our starting point will be the MNLS equation for the evolution of the complex envelope  $u(t, x)$  of the sea surface in deep water [18], in terms of which the surface elevation reads  $\eta(t, x) = \Re(u(t, x)e^{i(k_0x - \omega_0t)})$  (here  $k_0$  denotes the carrier wave number,  $\omega_0 = \sqrt{gk_0}$ , and  $g$  is the gravitational acceleration). Measuring  $u$  and  $x$  in units of  $k_0^{-1}$  and  $t$  in  $\omega_0^{-1}$  we can write MNLS in non-dimensional form as

$$\begin{aligned} \partial_t u + \frac{1}{2}\partial_x u + \frac{i}{8}\partial_x^2 u - \frac{1}{16}\partial_x^3 u + \frac{i}{2}|u|^2 u \\ + \frac{3}{2}|u|^2 \partial_x u + \frac{1}{4}u^2 \partial_x \bar{u} - \frac{i}{2}|\partial_x| |u|^2 = 0, \quad x \in [0, L], \end{aligned} \quad (1)$$

where the bar denotes complex conjugation. We will consider Eq. 1 with random initial condition  $u_0(x) \equiv u(0, x)$ , constructed via their Fourier representation,

$$u_0(x) = \sum_{n \in \mathbb{Z}} e^{ik_n x} (2\hat{C}_n)^{1/2} \theta_n, \quad \hat{C}_n = A e^{-k_n^2 / (2\Delta^2)}, \quad (2)$$

where  $k_n = 2\pi n/L$ ,  $\theta_n$  are complex Gaussian variables with mean zero and covariance  $\mathbb{E}\theta_n \bar{\theta}_m = \delta_{m,n}$ ,  $\mathbb{E}\theta_n \theta_m = \mathbb{E}\bar{\theta}_n \bar{\theta}_m = 0$ . This guarantees that  $u_0(x)$  is a Gaussian field with mean zero and  $\mathbb{E}(u_0(x)\bar{u}_0(x')) = 2 \sum_{n \in \mathbb{Z}} e^{ik_n(x-x')} \hat{C}_n$ . To make contact with the observational data, the amplitude  $A$  and the width  $\Delta$  in Eq. 2 are picked so that  $\hat{C}_n$  has the same height and area as the JONSWAP spectrum [31, 32] – see *Supporting Information* for details.

Because the initial data for Eq. 1 are random, so is the solution at time  $t > 0$ , and our aim is to compute

$$P_T(z) \equiv \mathbb{P}(F(u(T)) \geq z), \quad (3)$$

where  $\mathbb{P}$  denotes probability over the initial data and  $F$  is a scalar functional depending on  $u$  at time  $T > 0$ . Even though our method is applicable to more general observables, here we will focus on

$$F(u(T)) = \max_{x \in [0, L]} |u(T, x)|. \quad (4)$$

## II. LARGE DEVIATIONS THEORY APPROACH

A brute force approach to calculate Eq. 3 is Monte-Carlo sampling: Generate random initial conditions  $u_0(x)$  by picking random  $\theta_n$ 's in Eq. 2, evolve each of these  $u_0(x)$  deterministically via Eq. 1 up to time  $t = T$  to get  $u(T, x)$ , and count the proportion that fulfill  $F(u(T)) \geq z$ . While this method is simple, and will be used below as benchmark, it loses efficiency when  $z$  is large, which is precisely the regime of interest for the tails of the distribution of  $F(u(T))$ . In that regime, a more efficient approach is to rely on

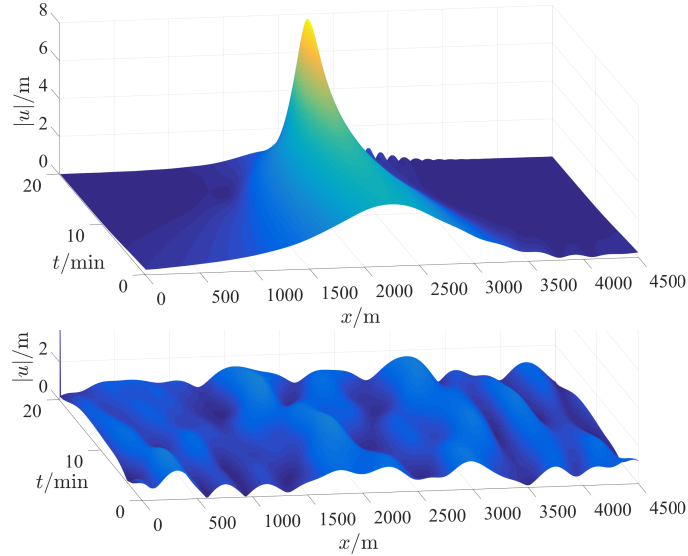


FIG. 1. *Top*: Time evolution of  $|u(t, x)|$  from an initial condition optimized for  $\max_x |u(T, x)| \geq 8$  m at  $T = 20$  min. *Bottom*: Same for a typical Gaussian random initial condition.

results from LDT which assert that Eq. 3 can be estimated by identifying the most likely initial condition that is consistent with  $F(u(T)) \geq z$ . To see how this result comes about, recall that the probability density of  $u_0$  is formally proportional to  $\exp(-\frac{1}{2}\|u_0\|_C^2)$ , where  $\|u_0\|_C^2$  is given by

$$\|u_0\|_C^2 = \sum_{n \in \mathbb{Z}} \frac{|\hat{a}_n|^2}{\hat{C}_n}, \quad \hat{a}_n = \frac{1}{L} \int_0^L e^{-ik_n x} u_0(x) dx. \quad (5)$$

To calculate Eq. 3 we should integrate this density over the set  $\Omega(z) = \{u_0 : F(u(T, u_0)) \geq z\}$ , which is hard to do in practice. Instead we can estimate the integral by Laplace's method. As shown in *Material and Methods*, this is justified for large  $z$ , when the probability of the set  $\Omega(z)$  is dominated by a single  $u_0(x)$  that contributes most to the integral and can be identified via the constrained minimization problem

$$\frac{1}{2} \min_{u_0 \in \Omega(z)} \|u_0\|_C^2 \equiv I_T(z), \quad (6)$$

which then yields the following LDT estimate for Eq. 3

$$P_T(z) \asymp \exp(-I_T(z)). \quad (7)$$

Here  $\asymp$  means that the ratio of the logarithms of both sides tends to 1 as  $z \rightarrow \infty$ . As discussed in *Material and Methods*, a multiplication prefactor can be added to (7) but it does not affect significantly the tail of  $P_T(z)$  on a logarithmic scale.

In practice, the constraint  $F(u(T, u_0)) \geq z$  can be imposed by adding a Lagrange multiplier term to Eq. 6, and it is easier to use this multiplier as control parameter and simply see *a posteriori* what value of  $z$

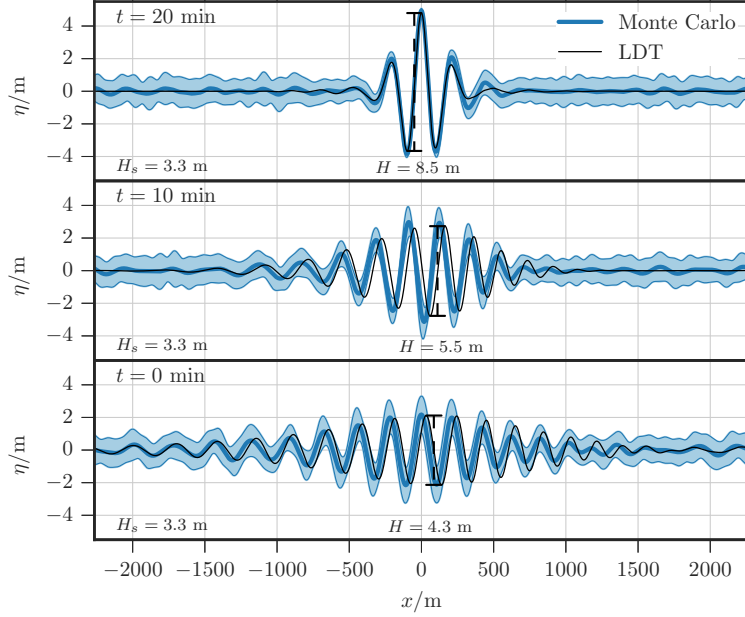


FIG. 2. Comparison between the average realization reaching  $\max_x |u(T, x)| \geq 4.8$  m at  $T = 20$  min (dark blue) and one standard deviation around this mean (light blue), with the solution reaching the same amplitude starting from the maximum likelihood initial condition (black) for  $t = 0, 10, 20$  min.

it implies. That is to say, perform for various values of  $\lambda$  the minimization

$$\min_{u_0} \left( \frac{1}{2} \|u_0\|_C^2 - \lambda F(u(T, u_0)) \right) \equiv S_T(\lambda), \quad (8)$$

over all  $u_0$  of the form in Eq. 2 (no constraint), then observe that this implies the parametric representation

$$I_T(z(\lambda)) = \frac{1}{2} \|u_0^*(\lambda)\|_C^2, \quad z(\lambda) = F(u(T, u_0^*(\lambda))). \quad (9)$$

where  $u_0^*(\lambda)$  denotes the minimizer obtained in Eq. 8. It is easy to see from Eqs. 6 and 8 that  $S_T(\lambda)$  is the Legendre transform of  $I_T(z)$  since:

$$S_T(\lambda) = \sup_{z \in \mathbb{R}} (\lambda z - I_T(z)) = \sup_{z \in \mathbb{R}} \left( \lambda z - \frac{1}{2} \inf_{u_0 \in \Omega(z)} \|u_0\|_C^2 \right), \quad (10)$$

### III. RESULTS

We considered two sets of parameters. In Set 1 we took  $A = 5.4 \cdot 10^{-5} k_0^{-2}$  and  $\Delta = 0.19 k_0$ . Converting back into dimensional units using  $k_0^{-1} = 36$  m consistent with the JONSWAP spectrum [31, 32], this implies a significant wave height  $H_s = 4\sqrt{C(0)} = 3.3$  m classified as a *rough sea* [33]. It also yields a Benjamin-Feir index  $\text{BFI} = 2\sqrt{2C(0)}/\Delta = 0.34$ , [32, 34], meaning that the modulational instability of a typical

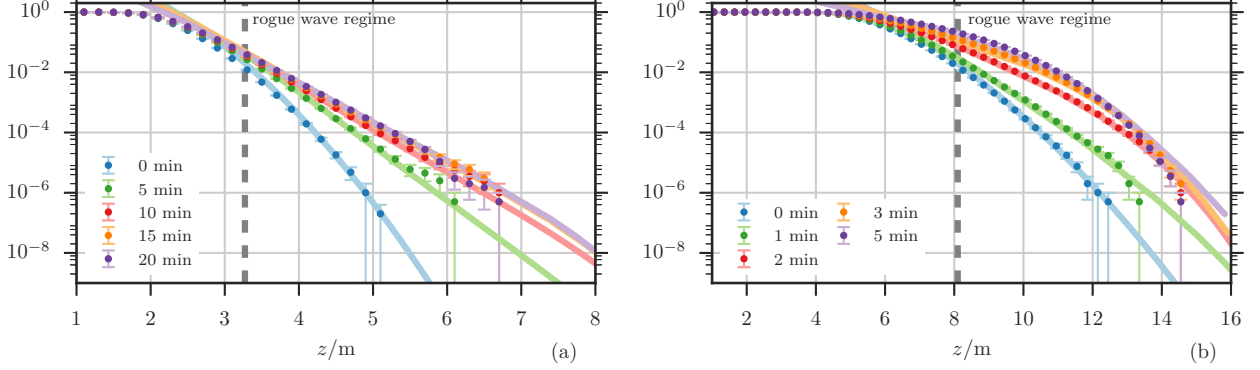


FIG. 3. Probabilities  $P_T(z)$  of  $\max_x |u(T, x)|$  for different times  $T$  for Set 1 (a) and Set 2 (b). The probabilities estimated by Monte-Carlo sampling with  $10^6$  realizations (dots) are compared with those predicted by LDT (lines). These probabilities agree over about 5 orders of magnitude in probability, though LDT allows for the calculation of the tail where Monte-Carlo becomes prohibitively costly. The error bars in the Monte-Carlo results represent the statistical error of 2 standard deviations (95% confidence interval) for the Bernoulli distribution with parameter  $P_T(z)$ .

initial condition is of medium intensity. In Set 2 we took  $A = 3.4 \cdot 10^{-4} k_0^{-2}$  and  $\Delta = 0.19 k_0$ , for which  $H_s = 8.2$  m is that of a *high sea* and the BFI is 0.85, meaning that the modulational instability of a typical initial condition is stronger.

Fig. 1 (top) shows the time evolution of  $|u(t, x)|$  starting from an initial condition from Set 1 optimized so that  $\max_x |u(T, x)| = 8$  m at  $T = 20$  min. For comparison, Fig. 1 (bottom) shows  $|u(t, x)|$  for a typical initial condition drawn from its Gaussian distribution. To illustrate what is special about the initial conditions identified by our optimization procedure, in Fig. 2 we show snapshots of the surface elevation  $\eta(t, x)$  at three different times,  $t = 0, 10, 20$  min (black lines), using the constraint that  $\max_x |u(T, x)| \geq 4.8$  m at  $T = 20$  min. Additionally, we averaged all Monte-Carlo samples achieving  $\max_x |u(t, x)| \geq 4.8$  m, translated to the origin. Snapshots of this mean configuration are shown in Fig. 2 (blue lines). They agree well with those of the optimized solution (black lines). The one standard deviation spread around the mean Monte-Carlo realization (light blue) is reasonably small, especially around the rogue wave at final time. This indicates that the event  $\max_x |u(T, x)| \geq 4.8$  m is indeed realized with probability close to 1 by starting from the most likely initial condition consistent with this event, as predicted by LDT. The usefulness of LDT is confirmed in Figs. 3 (a,b) depicting the probabilities of  $\max_x |u(T, x)|$  for both Sets 1 and 2 calculated via LDT optimization (lines), compared to Monte-Carlo sampling (dots). As can be seen, the agreement is remarkable, especially in the tail corresponding to the rogue wave regime. As expected, the Monte-Carlo sampling becomes inaccurate in the tail, since there the probabilities are dominated by unlikely events. The LDT calculation, in contrast, remains efficient and accurate far in the tail.

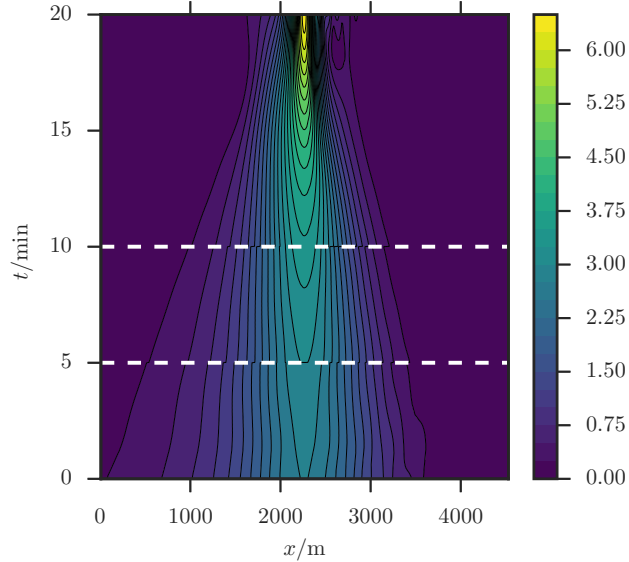


FIG. 4. Contourplot of the optimal trajectories from LDT for  $T = 10, 15,$  and  $20$  min in Set 1. The trajectories, superposed to match at  $t = T$ , coincide, which is consistent with the convergence of the probabilities  $P_T(z)$  for large  $T$ .

The probabilities plotted in Fig. 3 (a,b) show several remarkable features. First, they indicate that, as  $T$  gets larger, their tails fatten significantly. For example, in Set 1  $P_{T=20\text{ min}}(6\text{ m}) \approx 10^{-5}$ , which is 5 orders of magnitude larger than initially,  $P_{t=0\text{ min}}(6\text{ m}) \approx 10^{-10}$ . Secondly, the probabilities converge to a limiting density for large  $T$ . This occurs after some decorrelation time  $\tau_c \approx 10$  min in Set 1 and  $\tau_c \approx 3$  min in Set 2. Similarly, the LDT results converge. In fact, this convergence can be observed at the level of the trajectories generated from the optimal  $u_0^*$ . As Fig. 4 shows, reading these trajectories backward from  $t = T$ , their end portions coincide, regardless on whether  $T = 20$  min,  $T = 15$  min, or  $T = 10$  min. The implications of these observations, in particular on the mechanism of creation of rogue waves and their probability of appearance within a time window, will be discussed in *Interpretation* below.

Before doing so, let us discuss the scalability of our results to larger domain sizes, referring the reader to the *Supporting Information* for more details. As shown above, the optimization procedure based on large deviation theory predicts that the most likely way a rogue wave will occur in the domain is via the apparition of a single large peak in  $|u(t, x)|$ . In the set-up considered before, this prediction is confirmed by the brute-force simulations using Monte-Carlo sampling. It is clear, however, that for increased domain size, e.g. by taking a domain size of  $NL$  with  $N \gg 1$ , it will become increasingly likely to observe multiple peaks, for the simple reason that large waves can occur independently at multiple sufficiently separated locations. In these large domains, the large deviation predictions remain valid if we look at the maximum of  $|u(t, x)|$  in obser-

vation windows that are not too large (that is, about the size of the domain  $L$  considered above). However, they deteriorate if we consider this maximum in the entire domain of size  $NL$ , in the sense that the value  $\mathbb{P}(\max_{x \in [0, NL]} |u(t, x)| \geq z)$  predicted by large deviation theory matches that from Monte-Carlo sampling at values of  $z$  that are pushed further away in the tails. This is an entropic effect, which is easy to correct for: events in different subwindows must be considered independent, and their probabilities superposed. That is, if we denote by

$$P_T^N(z) = \mathbb{P}\left(\max_{x \in [0, NL]} |u(T, x)| \geq z\right), \quad (11)$$

it can be related to  $P_T(z) = \mathbb{P}(\max_{x \in [0, L]} |u(T, x)| \geq z)$  via

$$P_T^N(z) = 1 - (1 - P_T(z))^N. \quad (12)$$

This formula is derived in the *Supporting Information* and shown to accurately explain the numerical results. For efficiency  $L$  is chosen to be the smallest domain size for which boundary effects can be neglected, in the sense that the shape of the optimal trajectories does no longer change if  $L$  is increased further. In effect, this provides us with a method to scale up our results to arbitrary large observation windows.

#### IV. INTERPRETATION

The convergence of  $P_T(z)$  towards a limiting function  $P(z)$  has important consequences for the significance and interpretation of our method and its results. Notice first that this convergence can be explained if we assume that the probability distribution of the solutions to Eq. 1 with Gaussian initial data converges to an invariant measure. In this case, for large  $T$ , the Monte-Carlo simulations will sample the value of  $\max_x |u|$  on this invariant measure, and the optimization procedure based on LDT will do the same. The timescale  $\tau_c$  over which convergence occurs depends on how far this invariant measure is from the initial Gaussian measure of  $u_0(x)$ . Interestingly the values we observe for  $\tau_c$  are in rough agreement with the time scales predicted by the semi-classical limit of NLS that describes high-power pulse propagation [35, 36]. As recalled in the *Supporting Information*, this approach predicts that the timescale of apparition of a focusing solution starting from a large initial pulse of maximal amplitude  $U_i$  and length-scale  $L_i$  is  $\tau_c = \sqrt{T_{\text{nl}} T_{\text{lin}}}$ , where  $T_{\text{nl}} = (\frac{1}{2}\omega_0 k_0^2 U_i^2)^{-1}$  is the nonlinear timescale for modulational instability and  $T_{\text{lin}} = 8\omega_0^{-1} k_0^2 L_i^2$  is the linear timescale associated to group dispersion. Setting  $U_i = H_s$  (the size at the onset of rogue waves) and  $L_i = \sqrt{2\pi}\Delta^{-1}$  (the correlation length of the initial field) gives  $\tau_c \simeq 18$  min for Set 1 and  $\tau_c \simeq 8$  min for Set 2, consistent with the convergence times of  $P_T(z)$ . This observation has implications in terms of the mechanism of apparition of rogue waves, in particular their connection to the so-called Peregrine soliton,

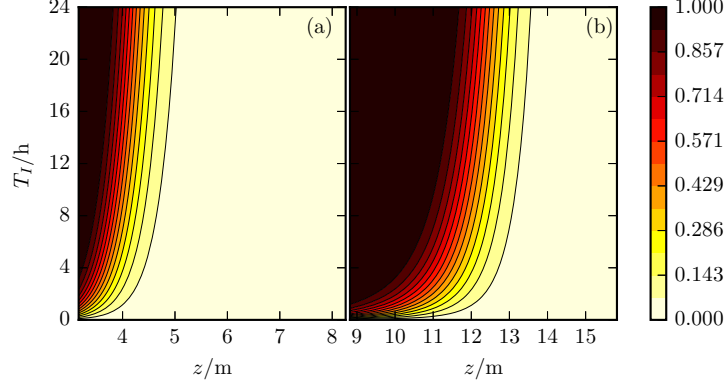


FIG. 5. Contourplots of the probability to observe a wave whose amplitude exceeds  $z$  in the time window  $[0, T_I]$  for Sets 1 (a) and 2 (b).

that has been invoked as prototype mechanism for rogue waves creation [5, 13, 37–40], in particular for water waves [24, 25, 41], plasmas [42] and fiber optics [36, 43, 44]. This connection is discussed in the *Supporting Information*.

Our findings also indicate that, even though the assumption that  $u_0(x)$  is Gaussian is incorrect in the tail (that is,  $P_{T=0}(z)$  is not equal to the limiting  $P(z)$  in the tail), it contains the right seeds to estimate  $P(z)$  via  $P_T(z)$  if  $T \gtrsim \tau_c$  [? ]. Altogether this is consistent with the scenario put forward by Sapsis and collaborators in [45, 46] to explain how extreme events arise in intermittent dynamical systems and calculate their probability: they occur when the system hits small instability pockets which trigger a large transient excursion. In this scenario, as long as the initial probability distribution in these pockets is accurate, the dynamics will permit precise estimation of the distribution tail. In some sense, the distribution of the initial condition plays a role of the prior distribution in Bayesian inference[? ], and the posterior can be effectively sampled by adding the additional information from the dynamics over short periods of time during which instabilities can occur. In [45], this picture was made predictive by using a two-dimensional ansatz for the initial condition  $u_0(x)$  to avoid having to perform sampling in high-dimension over the original  $u_0(x)$ . What our results show is that this approximation can be avoided altogether by using LDT to perform the calculations directly with the full Gaussian initial condition in Eq. 2.

Interestingly, we can use the results above to calculate the probability of occurrence of rogue waves in a given time window. More precisely, the probability  $p(z, T_I)$  that a rogue wave of amplitude larger than  $z$  be observed in the domain  $[0, L]$  during  $[0, T_I]$  (i.e. that  $\max_{t \in [0, T_I]} \max_{x \in [0, L]} |u(t, x)| \geq z$ ) can be estimated in terms of  $P(z)$  and  $\tau_c$  as

$$p \equiv \mathbb{P} \left( \max_{t \in [0, T_I]} \max_{x \in [0, L]} |u(t, x)| \geq z \right) \sim 1 - (1 - P(z))^{T_I/\tau_c}, \quad (13)$$

where we used the fact that rogue waves can be considered independent on timescales larger than  $\tau_c$  and assumed  $T_I \gg \tau_c$ . The function  $p$  is plotted in Fig. 5 as a function of  $z$  and  $T_I$ . For example for Set 1, Eq. 13 indicates a 50% chance to observe a rogue wave of height  $z = 4$  m (that is, about 8 m from crest-to-trough) after 11 hours (using  $\tau_c = 10$  min and  $P(z = 4 \text{ m}) = 1.1 \cdot 10^{-2}$ ); if we wait 30 hours, the chance goes up to 85%. Similarly, for Set 2 the chance to observe a wave of 11 m height is about 50% after 3 hours and about 85% after 8 hours ( $\tau_c = 3$  min and  $P(z = 11 \text{ m}) = 1.2 \cdot 10^{-2}$ ).

## V. CONCLUDING REMARKS

We have shown how an optimization problem building on LDT can be used to predict the pathway and likelihood of appearance of rogue waves in the solutions of MNLS fed by random initial data consistent with observations. This setup guarantees accuracy of the core of the initial distribution, which in turn permits the precise estimation of its tail via the dynamics. Our results give quantitative estimate for the probabilities of observing high amplitude waves within a given time window. These results also show that rogue waves have very specific precursors, a feature that was already noted in [47] in the context of a reduced model and could potentially be used for their early detection.

## VI. MATERIALS AND METHODS

### A. Laplace method and large deviations

For the reader's convenience, here we recall some standard large deviations results that rely on the evaluation of Gaussian integrals by Laplace's method and are at the core of the method we propose. It is convenient to rephrase the problem abstractly and consider the estimation of

$$P(z) = \mathbb{P}(\phi(\theta) > z), \quad (14)$$

where  $\theta \in \mathbb{R}^D$  are Gaussian random variables with mean zero and covariance Id, and  $\phi : \mathbb{R}^D \rightarrow \mathbb{R}$  is some real valued function – as long as we truncate the sum in Eq. 2 to a finite number of modes,  $|n| \leq M$ , the problem treated in this paper can be cast in this way, with  $\theta$  playing the role of  $C^{-1/2}u_0$  and  $\phi(\cdot)$  that of  $F(u(T, C^{-1/2}\cdot))$ . The probability  $P(z)$  in Eq. 14 is given by

$$P(z) = (2\pi)^{-D/2} \int_{\Omega(z)} e^{-\frac{1}{2}|\theta|^2} d\theta, \quad (15)$$

where  $\Omega(z) = \{\theta : \phi(\theta) > z\}$ . The interesting case is when this set does not contain the origin,  $0 \notin \Omega(z)$ , which we will assume is true when  $z > 0$ . We also make two additional assumptions:

1. The point on the boundary  $\partial\Omega(z)$  that is closest to the origin is isolated: Denoting this point as

$$\theta^*(z) = \operatorname{argmin}_{\theta \in \partial\Omega(z)} |\theta|^2, \quad (16)$$

we assume that

$$\begin{aligned} \frac{1}{2}|\theta^*(z)|^2 \text{ is strictly increasing with } z \geq 0; \\ \lim_{z \rightarrow \infty} \frac{1}{2}|\theta^*(z)|^2 = \infty. \end{aligned} \quad (17)$$

2. The connected piece of  $\partial\Omega(z)$  that contains  $\theta^*(z)$  is smooth with a curvature that is bounded by a constant independent of  $z$ .

The point  $\theta^*(z)$  satisfies the Euler-Lagrange equation for Eq. 16, with the constraint incorporated via a Lagrange multiplier term:

$$\theta^*(z) = \lambda \nabla \phi(\theta^*(z)) \quad (18)$$

for some Lagrange multiplier  $\lambda$ . This implies that

$$\frac{\theta^*(z)}{|\theta^*(z)|} = \frac{\nabla \phi(\theta^*(z))}{|\nabla \phi(\theta^*(z))|} = \hat{n}(z). \quad (19)$$

where  $\hat{n}(z)$  denotes the inward pointing unit vector normal to  $\partial\Omega(z)$  at  $\theta^*(z)$ . If we move inside the set  $\Omega(z)$  from  $\theta^*(z)$  in the direction of  $\hat{n}(z)$ , the norm  $|\theta|^2$  increases under the assumptions in Eq. 17. Indeed, setting  $\theta = \theta^*(z) + \hat{n}(z)u$  with  $u \geq 0$ , we have

$$\begin{aligned} |\theta|^2 &= |\theta^*(z)|^2 + 2\langle \hat{n}(z), \theta^*(z) \rangle u + u^2 \\ &= |\theta^*(z)|^2 + 2|\theta^*(z)|z + z^2, \end{aligned} \quad (20)$$

where we used Eq. 19. In fact, if we were to perform the integral in that direction, the natural variable of integration would be to rescale  $u \rightarrow u/|\theta^*(z)|$ . In particular, if we were to replace  $\Omega(z)$  by the half space  $P(z) = \{\theta \mid \hat{n}(z) \cdot (\theta - \theta^*(z)) > 0\}$ , it would be easy to estimate the integral in Eq. 15 by introducing a local coordinate system around  $\theta^*(z)$ , whose first coordinate is in the direction of  $\hat{n}(z)$ . Indeed this would give:

$$\begin{aligned} &(2\pi)^{-D/2} \int_{P(z)} e^{-\frac{1}{2}|\theta|^2} d\theta \\ &= (2\pi)^{-D/2} \int_0^\infty e^{-\frac{1}{2}|\theta^*(z)|^2 - |\theta^*(z)|u - \frac{1}{2}u^2} du \int_{\mathbb{R}^{N-1}} e^{-\frac{1}{2}|\eta|^2} d\eta \\ &= (2\pi)^{-1/2} e^{-\frac{1}{2}|\theta^*(z)|^2} \int_0^\infty e^{-|\theta^*(z)|u - \frac{1}{2}u^2} du \\ &= (2\pi)^{-1/2} |\theta^*(z)|^{-1} e^{-\frac{1}{2}|\theta^*(z)|^2} \int_0^\infty e^{-v - \frac{1}{2}|\theta^*(z)|^{-2}v^2} dv \\ &\sim (2\pi)^{-1/2} |\theta^*(z)|^{-1} e^{-\frac{1}{2}|\theta^*(z)|^2} \quad \text{as } z \rightarrow \infty. \end{aligned} \quad (21)$$

The last approximation goes beyond a large deviations estimate (i.e. it includes the prefactor), and it implies

$$\lim_{z \rightarrow \infty} |\theta^*(z)|^{-2} \log \left( (2\pi)^{-D/2} \int_{P(z)} e^{-\frac{1}{2}|\theta|^2} d\theta \right) = -\frac{1}{2}. \quad (22)$$

This log-asymptotic estimate is often written as

$$\int_{P(z)} e^{-\frac{1}{2}|\theta|^2} d\theta \asymp e^{-\frac{1}{2}|\theta^*(z)|^2} \quad \text{as } z \rightarrow \infty. \quad (23)$$

Interestingly, while the asymptotic estimate in Eq. 21 does not necessarily apply to the original integral in Eq. 15 (that is, the prefactor may take different forms depending on the shape of  $\partial\Omega(z)$  near  $\theta^*(z)$ ), the rougher log-asymptotic estimate in Eq. 23 does as long as the the boundary  $\partial\Omega(z)$  is smooth, with a curvature that is bounded by a constant independent of  $z$ . This is because because the contribution (positive or negative) to the integral over the region between  $\Omega(z)$  and  $P(z)$  is subdominant in that case, in the sense that the log of its amplitude is dominated by  $|\theta^*(z)|$ . This is the essence of the large deviations result that we apply in this paper.

## B. Numerical aspects

To perform the calculations, we solved Eq. 1 with  $L = 40\pi$  and periodic boundary conditions, and checked that this domain is large enough to make the effect of these boundary conditions negligible (see *Supporting Information*). The spatial domain was discretized using  $2^{12}$  equidistant gridpoints, which is enough to resolve the solution of Eq. 1. To evolve the field  $u(t, x)$  in time we used a pseudo-spectral second order exponential time-differencing (ETD2RK) method [48, 49].

When performing the Monte-Carlo simulations, we used  $10^6$  realizations of the random initial data constructed by truncating the sum in Eq. 2 over the  $M = 23$  modes with  $-11 \leq n \leq 11$ , i.e  $-3\Delta \leq k_n \leq 3\Delta$ : these modes carry most of the variance, and we checked that adding more modes to the initial condition did not affect the results in any significant way (see *Supporting Information*).

## C. Optimization procedure

As explained above, the large deviation rate function  $I_T(z)$  in Eq. 6 can be evaluated by solving the dual optimization problem in Eq. 8, which we rewrite as  $S_T(\lambda) = \inf_{u_0} E(u_0, \lambda)$ , where we defined the cost function

$$E(u_0, \lambda) \equiv \frac{1}{2} \|u_0\|_C^2 - \lambda F(u(T, u_0)). \quad (24)$$

We performed this minimization using steepest descent with adaptive step (line-search) and preconditioning of the gradient [50]. This involves evaluating the (functional) gradient of  $E_T(u_0, \lambda)$  with respect to  $u_0$ . Using the chain rule, this gradient can be expressed as (using compact vectorial notation)

$$\frac{\delta E}{\delta u_0} = C^{-1}u_0 - \lambda J^T(T, u_0) \frac{\delta F}{\delta u} \quad (25)$$

where  $J(t, u_0) = \delta u(t, u_0)/\delta u_0$  is the Jacobian of the transformation  $u_0 \rightarrow u(t, u_0)$ . Collecting all terms on the right-hand-side of the MNLS Eq. 1 into  $b(u)$ , this equation can be written as

$$\partial_t u = b(u), \quad u(t=0) = u_0, \quad (26)$$

and it is easy to see that in this notation  $J(t, u_0)$  satisfies

$$\partial_t J = \frac{\delta b}{\delta u} J, \quad J(t=0) = \text{Id}. \quad (27)$$

Consistent with what was done in the Monte-Carlo sampling, to get the results presented above we truncated the initial data  $u_0$  over  $M = 23$  modes using the representation

$$u_0(x) = \sum_{n=-11}^{11} e^{ik_n x} \hat{a}_n, \quad k_n = 2\pi n/L. \quad (28)$$

This means that minimization of Eq. 24 was performed in the  $2M - 1 = 45$  dimensional space spanned by the modes  $\hat{a}_n$ , accounting for invariance by an overall phase shift – to check convergence we also repeated this calculation using larger values of  $M$  and found no noticeable difference in the results (see *Supporting Information*).

In practice, the evaluation of the gradient in Eq. 25 was performed by integrating both  $u(t)$  and  $J(t)$  up to time  $t = T$ . Eq. 27 was integrated using the same pseudo-spectral method as for Eq. 1 on the same grid. To perform the steepest descent step, we then preconditioned the gradient through scalar multiplication by the step-independent, diagonal metric with the components of the spectrum  $\hat{C}_n$  as diagonal elements.

#### *Acknowledgment*

We thank W. Craig and M. Onorato for helpful discussions, and O. Bühler, M. Mohamad, and T. Sapsis for interesting comments. We also thank the anonymous reviewer for drawing our attention to the semi-classical theory for the Nonlinear Schrödinger Equation. GD is supported by the joint Math PhD program of Politecnico and Università di Torino. EVE is supported in part by the Materials Research Science and

Engineering Center (MRSEC) program of the National Science Foundation (NSF) under award number DMR-1420073 and by NSF under award number DMS-1522767.

---

- [1] Müller P, Garrett C, Osborne A (2005) Rogue waves. *Oceanography* 18(3):66.
- [2] White BS, Fornberg B (1998) On the chance of freak waves at sea. *J. Fluid Mech.* 355:113–138.
- [3] Haver S (2004) A possible freak wave event measured at the draupner jacket january 1 1995. *Rogue waves 2004* pp. 1–8.
- [4] Nikolkina I, Didenkulova I (2011) Rogue waves in 2006–2010. *Nat. Hazards Earth Syst. Sci.* 11(11):2913–2924.
- [5] Onorato M, Residori S, Bortolozzo U, Montina A, Arecchi F (2013) Rogue waves and their generating mechanisms in different physical contexts. *Phys. Rep.* 528(2):47–89.
- [6] Nazarenko S, Lukaschuk S (2016) Wave turbulence on water surface. *Annu. Rev. Condens. Matter Phys.* 7:61–88.
- [7] Akhmediev N, Soto-Crespo JM, Ankiewicz A (2009) Extreme waves that appear from nowhere: on the nature of rogue waves. *Physics Letters A* 373(25):2137–2145.
- [8] Akhmediev N, Pelinovsky E (2010) Editorial–introductory remarks on “discussion & debate: Rogue waves–towards a unifying concept?”. *Eur. Phys. J. Special Topics* 185(1):1–4.
- [9] Onorato M, Proment D, El G, Randoux S, Suret P (2016) On the origin of heavy-tail statistics in equations of the nonlinear schrödinger type. *Phys. Lett. A* 380(39):3173–3177.
- [10] Benjamin TB, Feir JE (1967) The disintegration of wave trains on deep water Part 1. Theory. *J. Fluid Mech.* 27(03):417–430.
- [11] Zakharov VE (1968) Stability of periodic waves of finite amplitude on the surface of a deep fluid. *J. Appl. Mech. Tech. Phys.* 9(2):190–194.
- [12] Kuznetsov EA (1977) Solitons in a parametrically unstable plasma. *Akademiia Nauk SSSR Doklady* 236:575–577.
- [13] Peregrine DH (1983) Water waves, nonlinear Schrödinger equations and their solutions. *The ANZIAM Journal* 25(01):16–43.
- [14] Akhmediev N, Eleonskii V, Kulagin N (1987) Exact first-order solutions of the nonlinear schrödinger equation. *Theoretical and mathematical physics* 72(2):809–818.
- [15] Osborne AR, Onorato M, Serio M (2000) The nonlinear dynamics of rogue waves and holes in deep-water gravity wave trains. *Phys. Lett. A* 275(5):386–393.
- [16] Zakharov VE, Ostrovsky LA (2009) Modulation instability: The beginning. *Physica D* 238(5):540–548.
- [17] Onorato M, et al. (2009) Statistical properties of directional ocean waves: the role of the modulational instability in the formation of extreme events. *Phys. Rev. Lett.* 102(11):114502.
- [18] Dysthe KB (1979) Note on a Modification to the Nonlinear Schrödinger Equation for Application to Deep Water Waves. *Proc. R. Soc. Lond. A* 369(1736):105–114.

- [19] Stiassnie M (1984) Note on the modified nonlinear schrödinger equation for deep water waves. *Wave motion* 6(4):431–433.
- [20] Trulsen K, Dysthe KB (1996) A modified nonlinear schrödinger equation for broader bandwidth gravity waves on deep water. *Wave motion* 24(3):281–289.
- [21] Craig W, Guyenne P, Sulem C (2010) A hamiltonian approach to nonlinear modulation of surface water waves. *Wave Motion* 47(8):552–563.
- [22] Gramstad O, Trulsen K (2011) Hamiltonian form of the modified nonlinear schrödinger equation for gravity waves on arbitrary depth. *J. Fluid Mech.* 670:404–426.
- [23] Onorato M, et al. (2004) Observation of strongly non-gaussian statistics for random sea surface gravity waves in wave flume experiments. *Phys. Rev. E* 70(6):067302.
- [24] Chabchoub A, Hoffmann N, Akhmediev N (2011) Rogue wave observation in a water wave tank. *Phys. Rev. Lett.* 106(20):204502.
- [25] Chabchoub A, Hoffmann N, Onorato M, Akhmediev N (2012) Super rogue waves: observation of a higher-order breather in water waves. *Phys. Rev. X* 2(1):011015.
- [26] Goulet A, Choi W (2011) A numerical and experimental study on the nonlinear evolution of long-crested irregular waves. *Phys. Fluids* 23(1):016601.
- [27] Lo E, Mei CC (1985) A numerical study of water-wave modulation based on a higher-order nonlinear schrödinger equation. *J. Fluid Mech.* 150:395–416.
- [28] Cousins W, Sapsis TP (2015) Unsteady evolution of localized unidirectional deep-water wave groups. *Phys. Rev. E* 91(6):063204.
- [29] Cousins W, Sapsis TP (2016) Reduced-order precursors of rare events in unidirectional nonlinear water waves. *J. Fluid Mech.* 790:368–388.
- [30] Nazarenko S (2011) *Wave turbulence*. (Springer Science & Business Media) Vol. 825.
- [31] Hasselmann K, et al. (1973) Measurements of wind-wave growth and swell decay during the joint north sea wave project (jonswap), (Deutsches Hydrographisches Institut), Technical report.
- [32] Onorato M, Osborne AR, Serio M, Bertone S (2001) Freak waves in random oceanic sea states. *Phys. Rev. Lett.* 86(25):5831.
- [33] Organization WM, ed. (2016) *Manual on Codes - International Codes, Volume I.1, Annex II to the WMO Technical Regulations: part A- Alphanumeric Codes*, WMO- No. 306. (Secretariat of the World Meteorological Organization).
- [34] Janssen PAEM (2003) Nonlinear Four-Wave Interactions and Freak Waves. *J. Phys. Oceanogr.* 33(4):863–884.
- [35] Bertola M, Tovbis A (2013) Universality for the focusing nonlinear schrödinger equation at the gradient catastrophe point: rational breathers and poles of the tritronquée solution to painlevé i. *Communications on Pure and Applied Mathematics* 66(5):678–752.
- [36] Tikan A, et al. (2017) Universality of the peregrine soliton in the focusing dynamics of the cubic nonlinear schrödinger equation. *Physical Review Letters* 119(3):033901.

- [37] Akhmediev N, Ankiewicz A, Taki M (2009) Waves that appear from nowhere and disappear without a trace. *Physics Letters A* 373(6):675–678.
- [38] Shrira VI, Geogjaev VV (2010) What makes the peregrine soliton so special as a prototype of freak waves? *Journal of Engineering Mathematics* 67(1):11–22.
- [39] Akhmediev N, Dudley JM, Solli D, Turitsyn S (2013) Recent progress in investigating optical rogue waves. *Journal of Optics* 15(6):060201.
- [40] Toenger S, et al. (2015) Emergent rogue wave structures and statistics in spontaneous modulation instability. *Scientific reports* 5.
- [41] Chabchoub A (2016) Tracking breather dynamics in irregular sea state conditions. *Physical review letters* 117(14):144103.
- [42] Bailung H, Sharma S, Nakamura Y (2011) Observation of peregrine solitons in a multicomponent plasma with negative ions. *Physical review letters* 107(25):255005.
- [43] Kibler B, et al. (2010) The peregrine soliton in nonlinear fibre optics. *Nature Physics* 6(10):790.
- [44] Suret P, et al. (2016) Single-shot observation of optical rogue waves in integrable turbulence using time microscopy. *Nature communications* 7.
- [45] Mohamad MA, Cousins W, Sapsis TP (2016) A probabilistic decomposition-synthesis method for the quantification of rare events due to internal instabilities. *J. Comp. Phys.* 322:288–308.
- [46] Farazmand M, Sapsis TP (2017) A variational approach to probing extreme events in turbulent dynamical systems. *arXiv preprint arXiv:1704.04116*.
- [47] Farazmand M, Sapsis TP (2017) Reduced-order prediction of rogue waves in two-dimensional deep-water waves. *Journal of Computational Physics* 340:418–434.
- [48] Cox SM, Matthews PC (2002) Exponential time differencing for stiff systems. *J. Comp. Phys.* 176(2):430–455.
- [49] Kassam AK, Trefethen LN (2005) Fourth-order time-stepping for stiff pdes. *SIAM J. Sci. Comput.* 26(4):1214–1233.
- [50] Borzì A, Schulz V (2011) *Computational optimization of systems governed by partial differential equations*. (SIAM).

# Supporting Information for “Rogue Waves and Large Deviations in Deep Sea ”

Giovanni Dematteis

*Courant Institute of Mathematical Sciences,  
New York University, New York, NY 10012, USA and  
Dipartimento di Scienze Matematiche, Politecnico di Torino,  
Corso Duca degli Abruzzi 24, I-10129 Torino, Italy*

Tobias Grafke

*Mathematics Institute, University of Warwick,  
Coventry CV4 7AL, United Kingdom*

Eric Vanden-Eijnden\*

*Courant Institute of Mathematical Sciences,  
New York University, New York, NY 10012, USA*

(Dated: December 13, 2017)

## I. CONSTRUCTION OF THE INITIAL CONDITION AND DYNAMICAL CONSISTENCY CHECK

Our procedure requires to specify the statistics of the (complex) envelope at initial time,  $u_0(x)$ , whereas the experimental spectrum is for the surface elevation  $\eta(x)$  which is related to  $u_0(x)$  as

$$\eta(x) = \Re(u_0(x)e^{ik_0x}), \quad (\text{S1})$$

To construct the initial  $u_0(x)$ , we introduce the auxiliary variable  $\zeta(x)$ ,<sup>5</sup>

$$\zeta(x) = \Im(u_0(x)e^{ik_0x}), \quad (\text{S2})$$

which we treat as a field independent of  $\eta(x)$ , with the same statistics. It is easy to see from Eqs. (S1) and (S2) that the envelope  $u_0(x)$  can then be expressed as

$$u_0(x) = (\eta(x) + i\zeta(x))e^{-ik_0x}. \quad (\text{S3})$$

Assuming that both  $\eta(x)$  and  $\zeta(x)$  are independent Gaussian fields with covariance  $\mathbb{E}(\eta(x)\eta(x')) = \mathbb{E}(\zeta(x)\zeta(x')) = C_\eta(x - x')$ , the envelope  $u_0(x)$  is also Gaussian, with covariance  $C_u(x - x') = \mathbb{E}(u(x)\bar{u}(x'))$  given by

$$C_u(x - x') = 2C_\eta(x - x')e^{-ik_0(x-x')}. \quad (\text{S4})$$

This relation implies that

$$\hat{C}_u(k) = 2\hat{C}_\eta(k + k_0). \quad (\text{S5})$$

where we defined

$$\hat{C}_u(k) = \frac{1}{2\pi} \int_{\mathbb{R}} e^{-ikx} C_u(x) dx, \quad \hat{C}_\eta(k) = \frac{1}{2\pi} \int_{\mathbb{R}} e^{-ikx} C_\eta(x) dx. \quad (\text{S6})$$

Recalling that  $k_0$  is defined as the wave vector at which the spectrum of  $\eta(x)$  should be centered, if we take a Gaussian ansatz for this spectrum, we should pick

$$\hat{C}_\eta(k) = \hat{C}_\eta(0)e^{-|k-k_0|^2/(2\Delta^2)}. \quad (\text{S7})$$

As a result,

$$\hat{C}_u(k) = 2\hat{C}_\eta(0)e^{-k^2/(2\Delta^2)}. \quad (\text{S8})$$

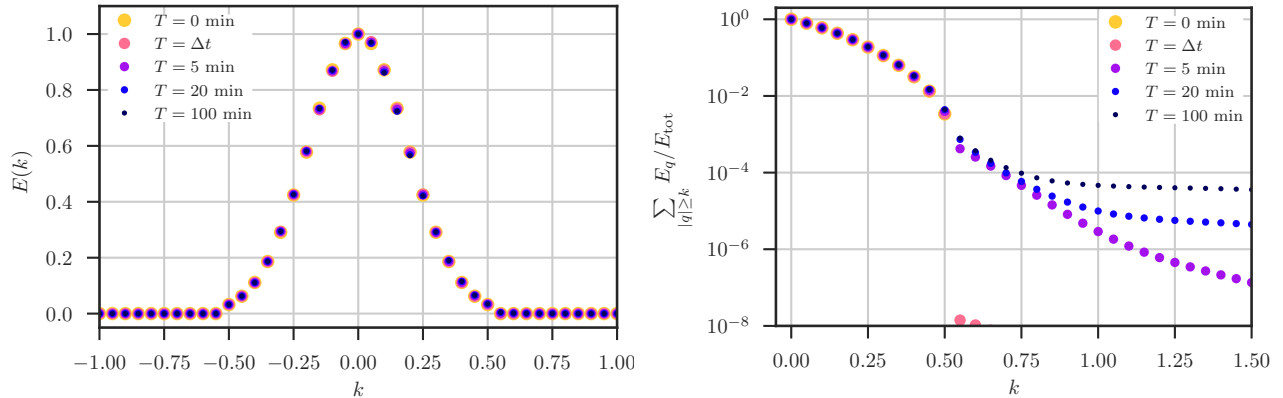


FIG. S1: Evolution of the spectrum of  $u(t, x)$ . The left panel shows that this spectrum stays essentially constant in time over 100 min, which justifies our choice of prior: indeed, from the viewpoint of this prior, the time evolution of  $u(t, x)$  leads to no changes. Of course, some features of  $u(t, x)$  change, as apparent from the evolution of other observables such as  $P_t(z) = \mathbb{P}(\max_x |u(t, x)|)$ : These changes can be detected in the spectrum, but they require us to look at much finer energy scales, as shown on the right panel where we plot the energy contained in modes above  $k > 0$  as  $k$  increases.

The spectrum for  $u_0(x)$  used in the paper is a discretized version of the one above, with  $A = (2\pi/L)^2 \hat{C}_\eta(0)$ .

The results reported in main text require us to evolve the field  $u(t, x)$  from its initial condition  $u_0(x)$ . As explained in main text, through this evolution, the probabilities  $P_t(z) = \mathbb{P}(\max_x |u(t, x)|)$  change with time  $t$  until they converge to some limit value. It is interesting to ask how much this evolution changes the prior information we used to construct the initial  $u_0(x)$ : that is, it is interesting to look at the spectrum of  $u(t, x)$  and see how much it differs from that of  $u_0(x)$ . The results of this calculation are shown in Fig. S1, and they indicate that the spectrum stays essentially constant in time over 100 min. This justifies our choice of prior: indeed, from the viewpoint of this prior, the time evolution of  $u(t, x)$  leads to no significant changes. Of course, some features of  $u(t, x)$  change, as apparent from the evolution of other observables such as  $P_t(z) = \mathbb{P}(\max_x |u(t, x)|)$ . Detecting the trace of these changes in the spectrum requires one to look at much finer energy scales: this can be seen on the right panel in Fig. S1 where we plot the energy contained in modes above  $k > 0$  for

increasing values of  $k$ .

## II. INFLUENCE OF THE SIZE OF THE DOMAIN AND OF THE OBSERVATION WINDOW

In this section, we investigate the influence of the size of the domain and/or that of the observation window on our results. To this end, we conduct experiments in domains of size  $L = L_0 = 40\pi$  (the domain size used in main text, which is  $L_0 \approx 4.53 \times 10^3$  m in dimensional units), and compare to  $L = 2L_0$ ,  $L = 4L_0$ , and  $L = 8L_0$ . The base domain size  $L_0$  was chosen to be as small as possible for computational efficiency, but still large enough that the influence of the periodic boundary conditions be negligible (as checked below). Consequently, *the results below can be interpreted either by thinking of  $L \geq L_0$  as the actual domain size, or as the size of the observation window in an even larger domain (including one that could be infinite)*. We also stress that our results are numerically converged and consistent in terms of numerical resolution, in the sense that we doubled both the number of gridpoints in the domain and the number of modes in the initial data each time we doubled the domain size. In particular, we used  $2^{12}$  gridpoints and  $M = 23$  initial modes ( $-11 \leq n \leq 11$ ) in the domain of size  $L$ ,  $2^{13}$  gridpoints and  $M = 47$  initial modes ( $-23 \leq n \leq 23$ ) in the domain of size  $2L$ , etc.

We begin by checking that the domain of size  $L_0 = 40\pi$  is already large enough to render negligible the effect of the boundary conditions. To this end, let us consider a different observable than the one in main text, namely the probability that  $|u(t, x)|$  be above a certain threshold at a given location  $x_0$  in the domain,

$$P_0^L(t, z) = \mathbb{P}(|u(t, x_0)| > z), \quad x_0 \in [0, L]. \quad (\text{S9})$$

By translational invariance,  $P_0^L(t, z)$  is independent of  $x_0$ . As  $L \rightarrow \infty$  this probability converges to a limiting value,  $P_0^L(t, z) \rightarrow P_0(t, z)$ , which makes it useful to consider here. As can be seen from Fig. S2, convergence is already achieved for  $L = L_0$ ,  $P_0^{L_0}(t, z) \approx P_0(t, z)$ . The results shown in Fig. S2 are for  $t = 15$  min, when the probability has converged to that on the invariant measure already. A similar conclusion can be made at intermediate times: Fig. S3 shows that doubling the domain size makes no significant difference, i.e.

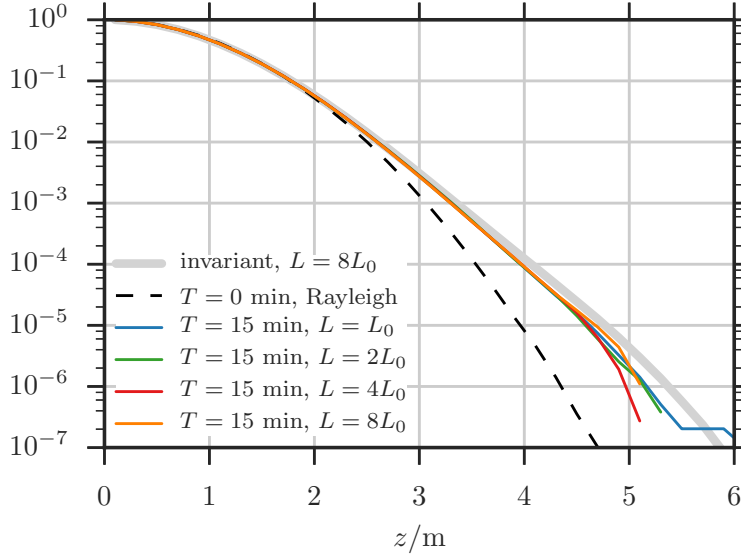


FIG. S2: Numerical verification of the invariance  $P_0^L(z) = \lim_{t \rightarrow \infty} P_0^L(t, z)$  for  $L \geq L_0$ . The limiting value  $P_0(z)$  (gray curve) was calculated by propagating 1500 samples up to time of 3000 min in the largest domain with  $L = 8L_0$ . Note that this also shows that  $P_0^{L_0}(t, z)$  in the MC sampling has essentially converged to the invariant  $P_0(z)$  after only 15 min.

$P_0^{2L_0}(t, z) \approx P_0^{L_0}(t, z)$ , both in the results from Monte-Carlo sampling and in those from our large deviation approach. The same invariance is also observed in the trajectories obtained by optimization in the large deviation approach, see Fig. S4. Note that these results are not surprising since  $L_0$  is already much larger than the correlation length of the initial field,  $L_0 \simeq 10L_c$  – this is in fact why this value of  $L_0$  was chosen to begin with.

Coming back to the quantity investigated in main text, let us denote

$$P_{\max}^L(t, z) = \mathbb{P} \left( \max_{x \in [0, L]} |u(t, x)| > z \right). \quad (\text{S10})$$

Unlike  $P_0^L(t, z)$ , the probability  $P_{\max}^L(t, z)$  does depend on  $L$  – the larger  $L$ , the higher  $P_{\max}^L(t, z)$ . We can actually estimate this growth explicitly. To see how, consider a domain of size  $NL$  that can be partitioned into  $N \geq 1$  sub-domains of size  $L$ , each large enough to be roughly statistically independent of the others. Then we have

$$1 - P_{\max}^{NL}(t, z) = (1 - P_{\max}^L(t, z))^N, \quad N \geq 1 \quad (\text{S11})$$

since in order for the maximum of  $|u|$  to be less than  $z$  in the larger domain of size  $NL$ , it must be less than  $z$  in each of the (roughly independent) sub-domains of size  $L$ . Eq. (S11)

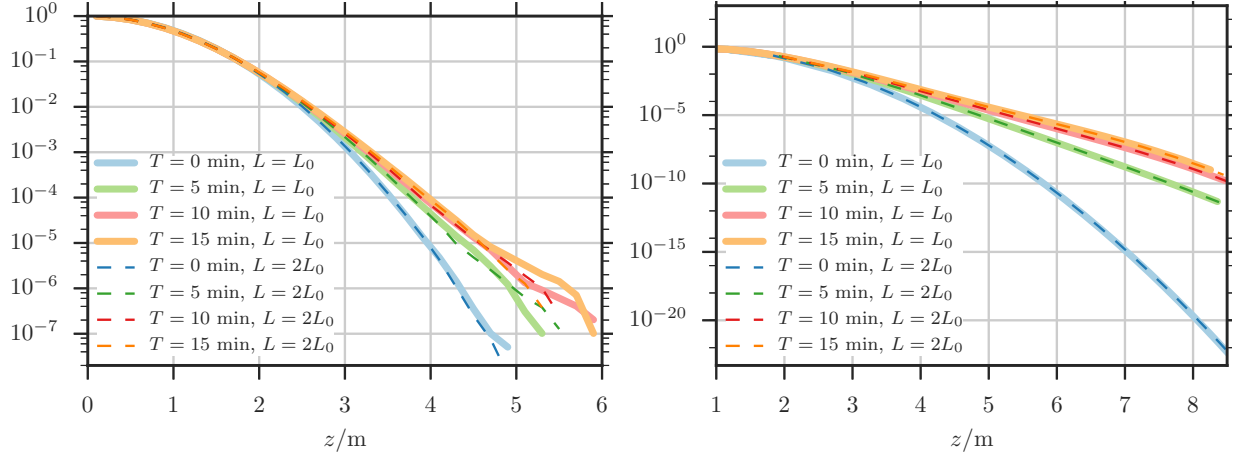


FIG. S3: Left:  $P_0^L(t, z) = \mathbb{P}(|u(t, x_0)| > z)$  at a fixed location  $x_0$  and different times  $t$  in domains of size  $L = L_0$  and  $L = 2L_0$  obtained by Monte Carlo (MC) sampling. Right: Same, obtained by optimization using our large deviation approach and a larger range of values for  $z$  (such large values cannot easily be reached by MC). As can be seen, the PDFs essentially lay on top of each other for the two different domains, confirming that the domain size  $L_0$  is large enough for the periodic boundary conditions to not affect the results.

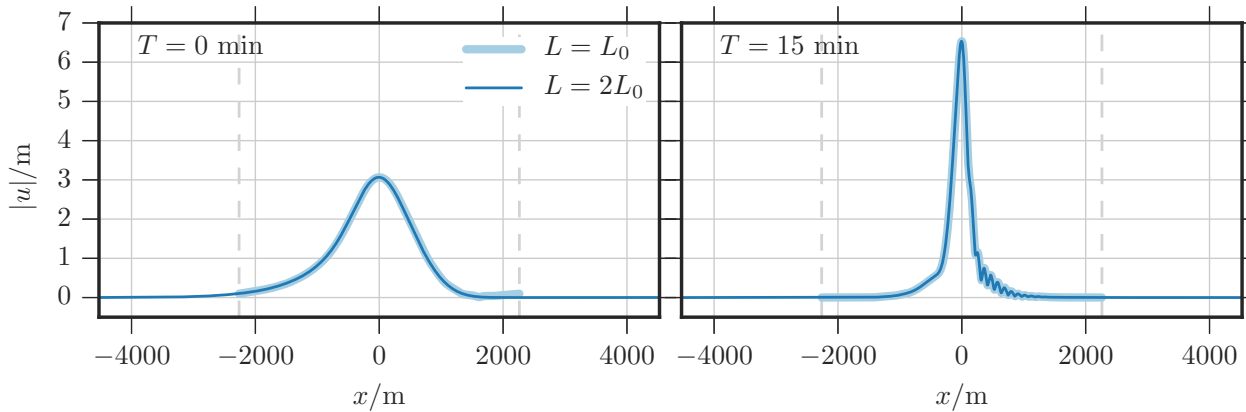


FIG. S4: Optimal trajectories calculated in the domains of size  $L = L_0$  (thick line) and  $L = 2L_0$  (thin line). As can be seen, the periodicity of the domain does not affect significantly the shape of the instanton inside this domain.

is the fundamental equation used in extreme value statistics. We confirmed its applicability for  $L = L_0 = 40\pi$  in our system via direct estimation of  $P_{\max}^{NL_0}(t, z)$  for  $N = 1, 2, 4, 8$  by Monte Carlo sampling. These results are reported in Fig. S5.

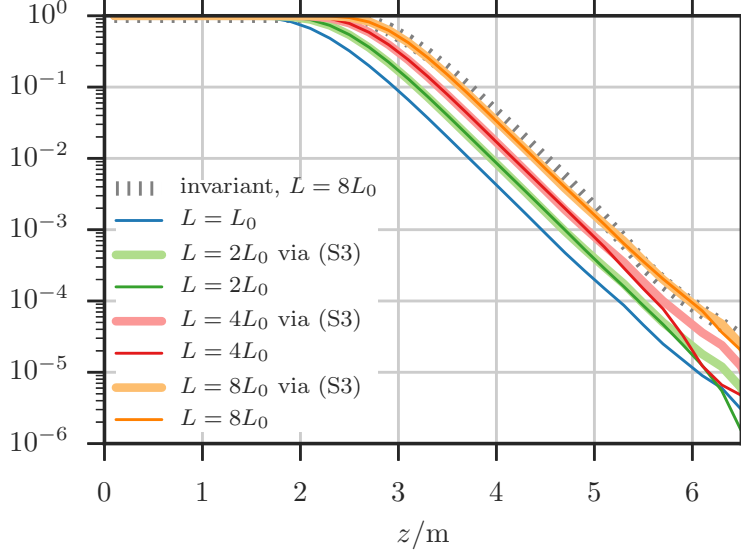


FIG. S5: Numerical verification of (S11) for  $L = L_0 = 40\pi$ . These results confirm that adjacent boxes of size  $L_0$  can be considered statistically independent. The probability  $P_{\max}^L(z) = \lim_{t \rightarrow \infty} P_{\max}^L(t, z)$  for  $L = 8L_0$ , is also shown, indicating that this quantity can be estimated accurately from  $P_{\max}^{L_0}$  at 15 min using (S11).

Since  $L_0 = 40\pi$  is already large enough for (S11) to hold, we can rewrite this equation as

$$1 - P_{\max}^L(t, z) = (1 - P_{\max}^{L_0}(t, z))^{L/L_0}, \quad L \geq L_0 \quad (\text{S12})$$

Note that this equation implies that, at fixed  $z$ ,  $P_{\max}^L(t, z)$  increases with  $L$  since  $1 - P_{\max}^{L_0}(t, z) < 1$  and therefore  $1 - P_{\max}^L(t, z) = (1 - P_{\max}^{L_0}(t, z))^{L/L_0} \leq 1 - P_{\max}^{L_0}(t, z)$  for  $L \geq L_0$ . Intuitively, this increase in  $P_{\max}^L(t, z)$  stems from the fact that multiple large values of  $|u|$  are expected to arise simultaneously in different sub-domains since they are statistically independent – this is usually referred to as an entropic effect, and it can be seen in the typical realizations from the Monte-Carlo sampling shown in Fig. S6 for  $L = L_0$  and  $L = 8L_0$ . Of course this effect is properly accounted for by Eq. (S11). Indeed, realizations like those shown in Fig. S6 are those from which the probabilities shown in Fig. S5 were calculated.

It is also important to stress that this entropic effect cannot be accounted for directly by our large deviation approach. The solution obtained by optimization becomes independent of  $L$  for  $L$  large enough (which is the case already for  $L = L_0$ ). This implies that, without correction, the results of the large deviation approach will deteriorate with increasing  $L$ .

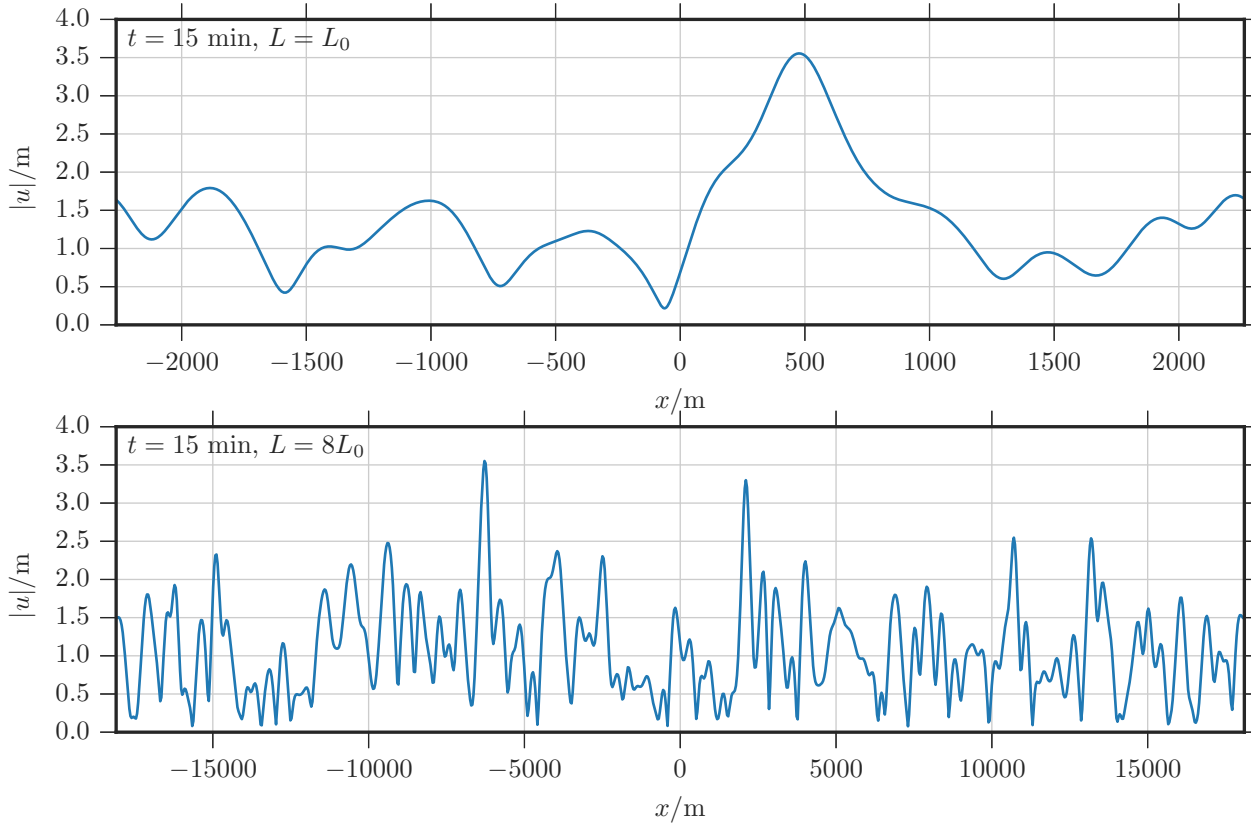


FIG. S6: Typical realizations from the Monte-Carlo sampling such that  $\max_x |u(t, x)| \geq 3.5$  m at  $t = 15$  min in the domains of size  $L = L_0$  (top) and  $L = 8L_0$  (bottom). As can be seen, as the domain size increases, it becomes increasingly likely to observe more than one large value of  $|u(t, x)|$  in the domain.

Eq. (S12) shows that this issue can be easily fixed, however: indeed this formula indicates how the large deviation results at  $L = L_0$  (i.e. in a domain that is large enough to not be influenced by the boundary condition, but small enough that the entropic effects remain negligible) can be extended to larger  $L$ .

### III. THE CASE OF THE NONLINEAR SCHRÖDINGER EQUATION (NLS) AND THE ROLE OF THE PEREGRINE SOLITON (PS)

For completeness, we redid all of our calculations in the context of the standard Nonlinear Schrödinger (NLS) equation instead of the MNLS equation. Using the same non-dimensional

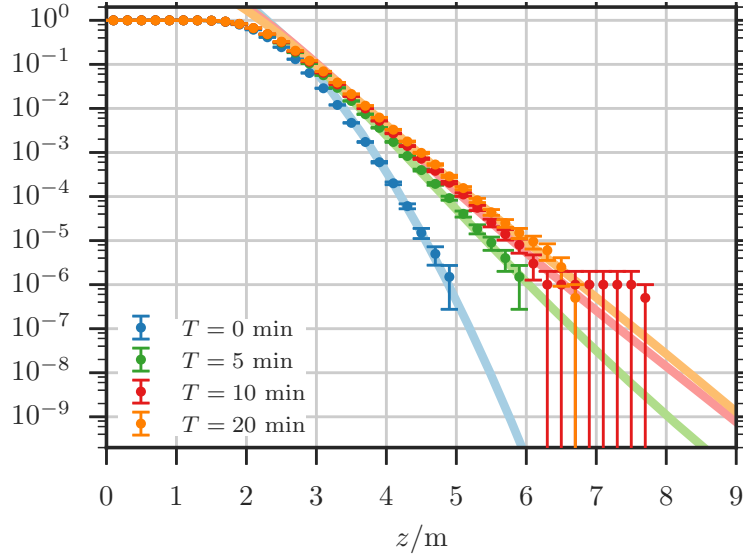


FIG. S7:  $\mathbb{P}(\max_x |u(t, x)| \geq z)$  for  $u(t, x)$  solution of NLS at different times calculated by Monte Carlo sampling using  $10^6$  realizations and compared to the results obtained via optimization in our large deviation approach.

variables as in MNLS, NLS reads

$$\partial_t u + \frac{i}{8} \partial_{xx} u + \frac{i}{2} u |u|^2 = 0. \quad (\text{S13})$$

Fig. S7 shows the distributions for the spatial maximum of the envelope  $|u|$  at different times calculated by both direct Monte-Carlo sampling and minimization using our large deviation approach, using the same random initial conditions as in MNLS. As can be seen, here too the approach based on large deviation theory does an excellent job at capturing these PDFs.

The advantage of using NLS is that it permits us to assess the relevance of the Peregrine soliton (PS), which is an exact solution of NLS (though not of MNLS) that has been invoked as prototype mechanism for rogue waves creation<sup>5,13,37-40</sup> – recent experimental results in the context of water waves<sup>24,25,41</sup>, plasmas<sup>42</sup> and fiber optics<sup>36,43,44</sup> have lent support to this hypothesis. The PS reads

$$u(t, x) = U_i e^{-it/T_{\text{nl}}} \left( \frac{4(1 - 2it/T_{\text{nl}})}{1 + 4(t/T_{\text{nl}})^2 + 4(x/L_{\text{nl}})^2} - 1 \right), \quad T_{\text{nl}} = \frac{2}{U_i^2}, \quad L_{\text{nl}} = \frac{1}{4} \sqrt{T_{\text{nl}}} = \frac{\sqrt{2}}{4U_i}, \quad (\text{S14})$$

where  $U_i > 0$  is a free parameter. It can be checked that this solution reaches its maximal amplitude  $|u(0, 0)| = 3U_i$  at  $(t, x) = (0, 0)$  and decays both forward and backward in time

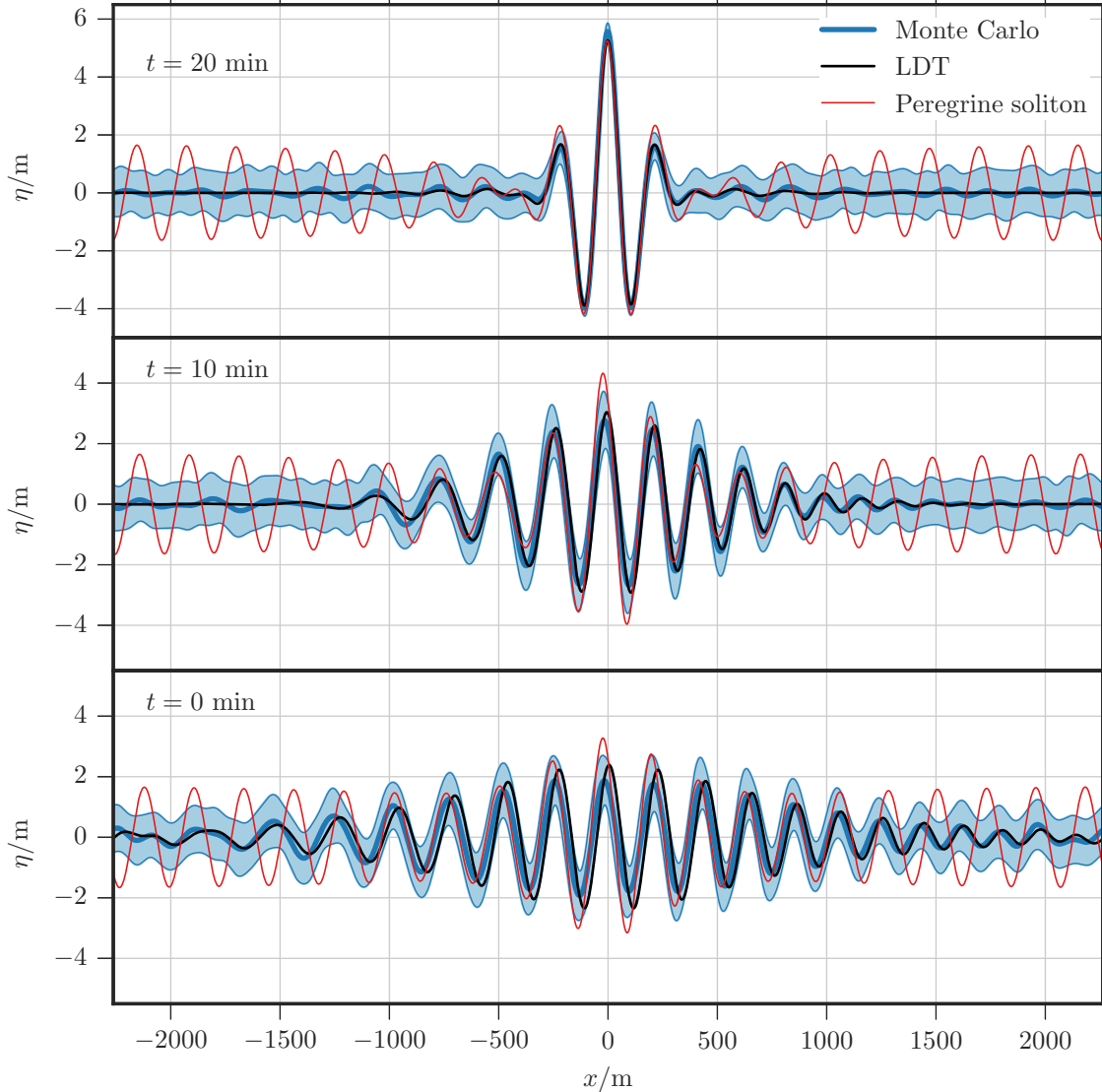


FIG. S8: Comparison of the optimized solution, the mean and standard deviation of the Monte-Carlo realizations, and the PS reaching the same maximal surface elevation at  $T = 20$  min. From bottom to top the figures are at 0, 10 and 20 minutes respectively, and these results are for NLS.

to  $\lim_{t \rightarrow \pm\infty} |u(t, x)| = U_i$ .

To compare the PS to our results, we translated  $t$  in (S14) to make the time at which this solution reaches its maximal amplitude coincide with the time at which a prescribed value of the wave elevation is observed in either our minimization procedure or in the MC sampling. By adjusting  $U_i$  so that the maximal amplitude of the PS also coincides with this prescribed value of the amplitude, we can then verify how well the PS reproduces our instanton as well as the mean and variance of the solutions observed in the MC sampling.

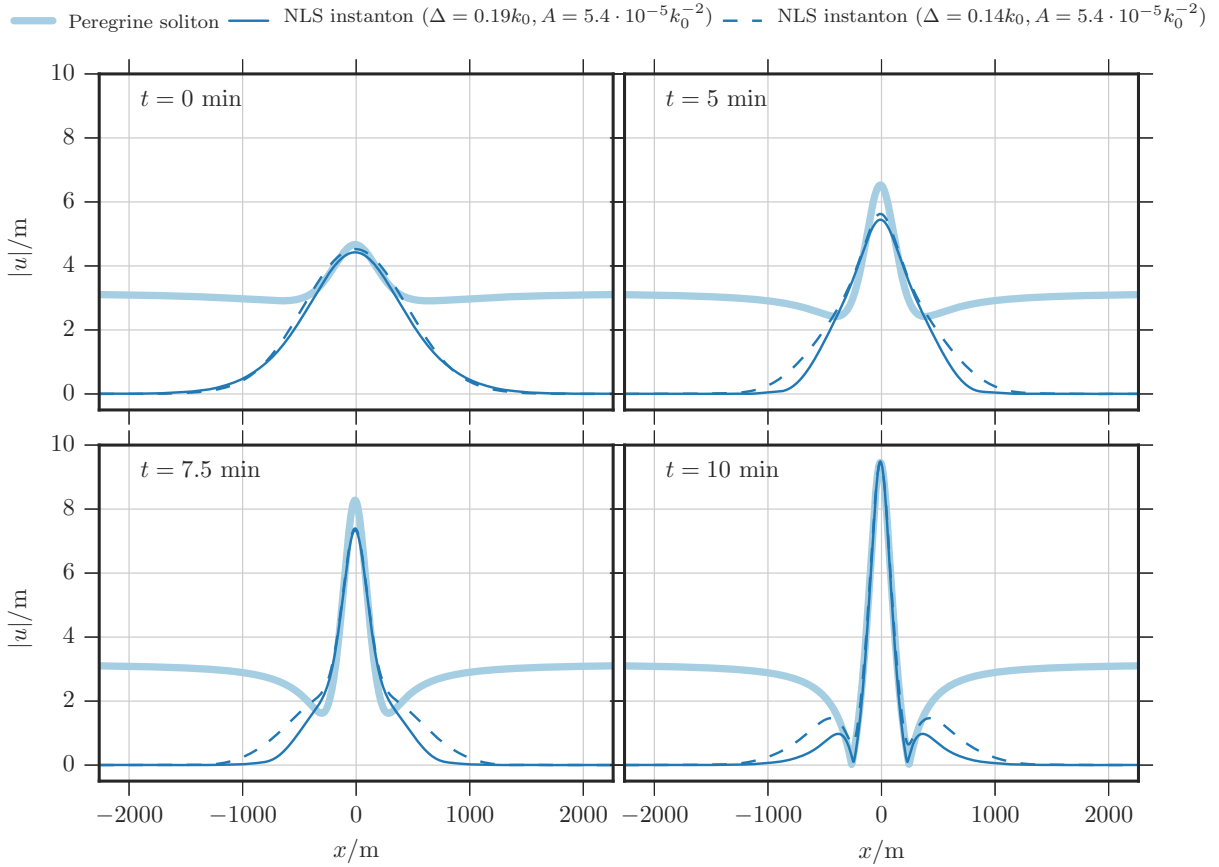


FIG. S9: Comparison between the optimized solution for a very extreme surface elevation and the PS reaching the same final height (after  $T = 10$  minutes). Comparison with realization from the Monte-Carlo sampling is impossible due to the extreme rareness of such event on the ensemble of the initial conditions. The evolution is shown at times 0 min, 5 min, 7.5 min, and 10 min, respectively. These results are for NLS.

These results are reported in Fig. S8. As can be seen, the PS captures the shape of the instanton at final time (i.e. when the rogue wave occurs) reasonably well, at least near the location  $x = 0$  where the maximum amplitude is observed (focusing region). The PS also does a reasonably good job at tracking the evolution of the solution that led to this extreme event. In particular, the focusing time scale of the optimized solutions (which we interpret to also describe the convergence time of the a-priori distribution to the invariant distribution) is in rough agreement with the effective focusing time scale of the PS starting from a pulse of size  $L_i$ <sup>36,44</sup>. This time scale is given by  $\tau_c = \sqrt{T_{nl}T_{lin}}$ , where the nonlinear

time  $T_{\text{nl}}$  is defined in (S14) and the linear time  $T_{\text{lin}} = 8L_i^2$  is that associated with group velocity dispersion of the initial pulse – in dimensional units, these are  $T_{\text{nl}} = (\frac{1}{2}\omega_0 k_0^2 U_i^2)^{-1}$  and  $T_{\text{lin}} = 8\omega_0^{-1} k_0^2 L_i^2$ .

The relative agreement both in shape and timescale between the optimized solution and the PS suggests that the main physical phenomenon responsible for the focusing in the NLS equation is the gradient catastrophe<sup>35</sup>, which fosters a very unique evolution pathway as the point of maximum focusing is approached in space-time. Still, it should be stressed that the discrepancies between the PS and the actual solution we observe become more and more pronounced backward in time. These differences can also be observed in Fig. S9 where we plot the amplitude of  $u$  for a more extreme event that is too rare to be observed by MC sampling. In this figure, we show the optimized solutions obtained for two different spectral widths  $\Delta$ , whose shapes are slightly different from one another: clearly, these differences cannot be captured by the PS since this solution is completely specified by the final amplitude, which is the same for both sets.

For completeness we also compared the PS with the solutions obtained in the context of MNLS. These results are reported on Fig. S10 and show similar type of agreement, in particular in term of the shape of the rogue wave near its maximum and the time scale of its emergence. Note the discrepancies between the PS and our solutions is even more pronounced in this case, which is to be expected since PS is an exact solution of NLS, but not of MNLS.

To summarize, while the PS can explain some features of the rogue waves, in particular their shape as well as the focusing time scale over which these waves evolve from a large initial pulse, it does not capture the details of the formation of these waves - indeed there is no reason why it should, since different sets of random initial conditions lead to waves with different shapes (and whose amplitudes have different statistics) and this information is not seen by the PS. In particular, the instanton solution for the initial data chosen here depends on two parameters, the significant wave height  $H_s$  and the BFI, while the PS only allows a single parameter  $U_i$ . Additionally and more importantly, the PS does not allow the estimation of the probability of observing rogue waves of given amplitude since this solution *per se* is devoid of a probabilistic framework.

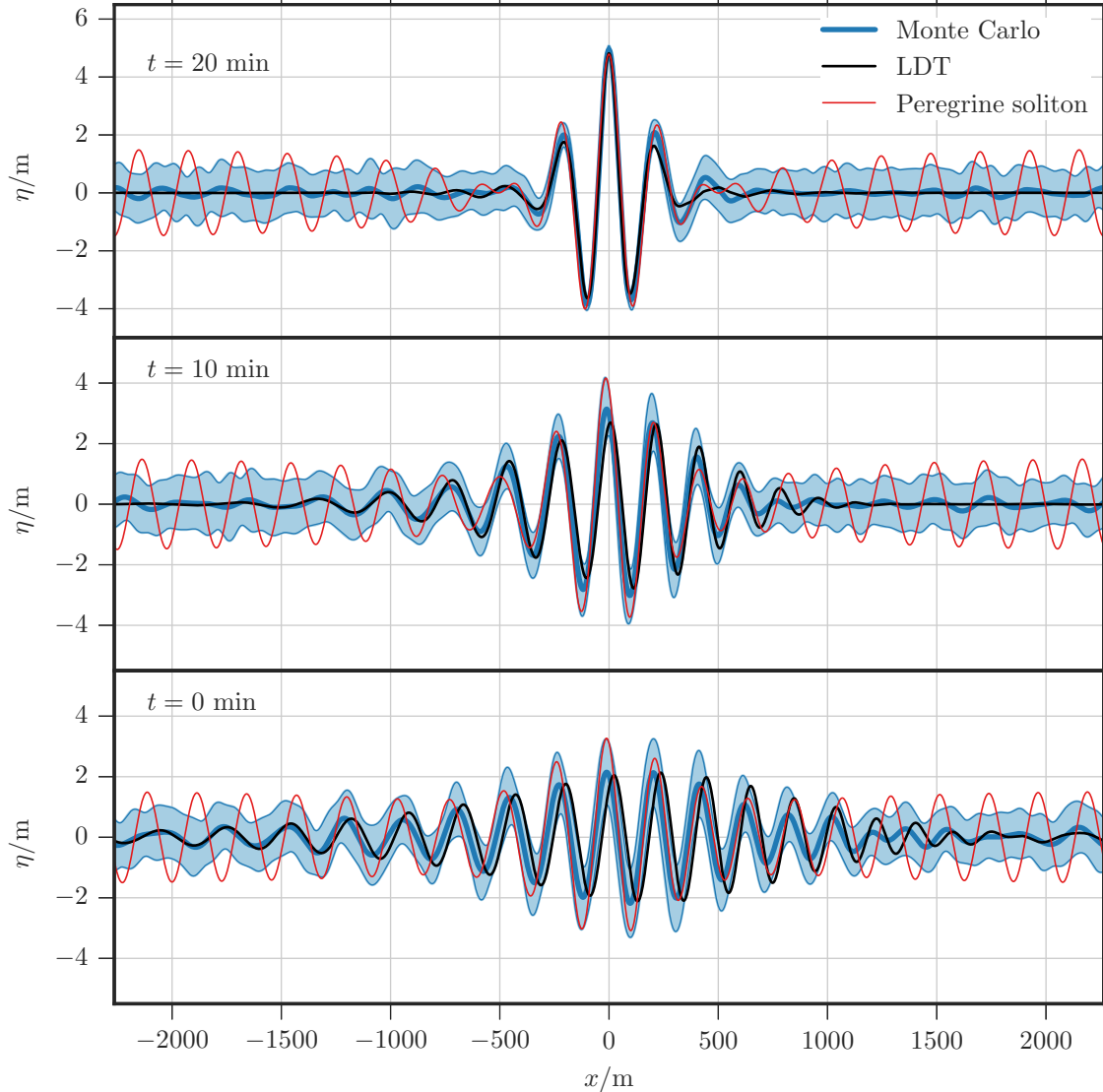


FIG. S10: Same as in Fig. S8 for MNLs.

### Video captions

*Video 1:* Time evolution of the surface elevation of the optimized solution and the PS reaching the same maximal amplitude  $\max_x |u(T, x)| = 5.25$  m at  $T = 20$  min, compared with that of the mean and standard deviation of the trajectories sampled by MC that reach  $\max_x |u(T, x)| \geq 5.25$  m. These calculations were performed in the context of the NLS equation, for which the PS is an exact solution.

*Video 2:* Comparison between two instantons and the PS reaching the same maximal amplitude  $\max_x |u(T, x)|$  m at  $T = 10$  min. The two instantons are optimized solutions for two

statistical states of the sea with a different spectral width  $\Delta$ . These calculations were performed in the context of the NLS equation, for which the PS is an exact solution. For the event shown here, the extreme size and rareness make comparison with the MC sampling impossible in practice.

---

\* Electronic address: eve2@cims.nyu.edu

- <sup>1</sup> Müller P, Garrett C, Osborne A (2005) Rogue waves. *Oceanography* 18(3):66.
- <sup>2</sup> White BS, Fornberg B (1998) On the chance of freak waves at sea. *J. Fluid Mech.* 355:113–138.
- <sup>3</sup> Haver S (2004) A possible freak wave event measured at the draupner jacket january 1 1995. *Rogue waves 2004* pp. 1–8.
- <sup>4</sup> Nikolkina I, Didenkulova I (2011) Rogue waves in 2006–2010. *Nat. Hazards Earth Syst. Sci.* 11(11):2913–2924.
- <sup>5</sup> Onorato M, Residori S, Bortolozzo U, Montina A, Arecchi F (2013) Rogue waves and their generating mechanisms in different physical contexts. *Phys. Rep.* 528(2):47–89.
- <sup>6</sup> Nazarenko S, Lukaschuk S (2016) Wave turbulence on water surface. *Annu. Rev. Condens. Matter Phys.* 7:61–88.
- <sup>7</sup> Akhmediev N, Soto-Crespo JM, Ankiewicz A (2009) Extreme waves that appear from nowhere: on the nature of rogue waves. *Physics Letters A* 373(25):2137–2145.
- <sup>8</sup> Akhmediev N, Pelinovsky E (2010) Editorial–introductory remarks on discussion & debate: Rogue waves–towards a unifying concept?. *Eur. Phys. J. Special Topics* 185(1):1–4.
- <sup>9</sup> Onorato M, Proment D, El G, Randoux S, Suret P (2016) On the origin of heavy-tail statistics in equations of the nonlinear schrödinger type. *Phys. Lett. A* 380(39):3173–3177.
- <sup>10</sup> Benjamin TB, Feir JE (1967) The disintegration of wave trains on deep water Part 1. Theory. *J. Fluid Mech.* 27(03):417–430.
- <sup>11</sup> Zakharov VE (1968) Stability of periodic waves of finite amplitude on the surface of a deep fluid. *J. Appl. Mech. Tech. Phys.* 9(2):190–194.
- <sup>12</sup> Kuznetsov EA (1977) Solitons in a parametrically unstable plasma. *Akademiia Nauk SSSR Doklady* 236:575–577.
- <sup>13</sup> Peregrine DH (1983) Water waves, nonlinear Schrödinger equations and their solutions. *The*

- ANZIAM Journal* 25(01):16–43.
- <sup>14</sup> Akhmediev N, Eleonskii V, Kulagin N (1987) Exact first-order solutions of the nonlinear schrödinger equation. *Theoretical and mathematical physics* 72(2):809–818.
- <sup>15</sup> Osborne AR, Onorato M, Serio M (2000) The nonlinear dynamics of rogue waves and holes in deep-water gravity wave trains. *Phys. Lett. A* 275(5):386–393.
- <sup>16</sup> Zakharov VE, Ostrovsky LA (2009) Modulation instability: The beginning. *Physica D* 238(5):540–548.
- <sup>17</sup> Onorato M, et al. (2009) Statistical properties of directional ocean waves: the role of the modulational instability in the formation of extreme events. *Phys. Rev. Lett.* 102(11):114502.
- <sup>18</sup> Dysthe KB (1979) Note on a Modification to the Nonlinear Schrödinger Equation for Application to Deep Water Waves. *Proc. R. Soc. Lond. A* 369(1736):105–114.
- <sup>19</sup> Stiassnie M (1984) Note on the modified nonlinear schrödinger equation for deep water waves. *Wave motion* 6(4):431–433.
- <sup>20</sup> Trulsen K, Dysthe KB (1996) A modified nonlinear schrödinger equation for broader bandwidth gravity waves on deep water. *Wave motion* 24(3):281–289.
- <sup>21</sup> Craig W, Guyenne P, Sulem C (2010) A hamiltonian approach to nonlinear modulation of surface water waves. *Wave Motion* 47(8):552–563.
- <sup>22</sup> Gramstad O, Trulsen K (2011) Hamiltonian form of the modified nonlinear schrödinger equation for gravity waves on arbitrary depth. *J. Fluid Mech.* 670:404–426.
- <sup>23</sup> Onorato M, et al. (2004) Observation of strongly non-gaussian statistics for random sea surface gravity waves in wave flume experiments. *Phys. Rev. E* 70(6):067302.
- <sup>24</sup> Chabchoub A, Hoffmann N, Akhmediev N (2011) Rogue wave observation in a water wave tank. *Phys. Rev. Lett.* 106(20):204502.
- <sup>25</sup> Chabchoub A, Hoffmann N, Onorato M, Akhmediev N (2012) Super rogue waves: observation of a higher-order breather in water waves. *Phys. Rev. X* 2(1):011015.
- <sup>26</sup> Goullet A, Choi W (2011) A numerical and experimental study on the nonlinear evolution of long-crested irregular waves. *Phys. Fluids* 23(1):016601.
- <sup>27</sup> Lo E, Mei CC (1985) A numerical study of water-wave modulation based on a higher-order nonlinear schrödinger equation. *J. Fluid Mech.* 150:395–416.
- <sup>28</sup> Cousins W, Sapsis TP (2015) Unsteady evolution of localized unidirectional deep-water wave groups. *Phys. Rev. E* 91(6):063204.

- <sup>29</sup> Cousins W, Sapsis TP (2016) Reduced-order precursors of rare events in unidirectional nonlinear water waves. *J. Fluid Mech.* 790:368–388.
- <sup>30</sup> Nazarenko S (2011) *Wave turbulence*. (Springer Science & Business Media) Vol. 825.
- <sup>31</sup> Hasselmann K, et al. (1973) Measurements of wind-wave growth and swell decay during the joint north sea wave project (jonswap), (Deutsches Hydrographisches Institut), Technical report.
- <sup>32</sup> Onorato M, Osborne AR, Serio M, Bertone S (2001) Freak waves in random oceanic sea states. *Phys. Rev. Lett.* 86(25):5831.
- <sup>33</sup> Organization WM, ed. (2016) *Manual on Codes - International Codes, Volume I.1, Annex II to the WMO Technical Regulations: part A- Alphanumeric Codes*, WMO- No. 306. (Secretariat of the World Meteorological Organization).
- <sup>34</sup> Janssen PAEM (2003) Nonlinear Four-Wave Interactions and Freak Waves. *J. Phys. Oceanogr.* 33(4):863–884.
- <sup>35</sup> Bertola M, Tovbis A (2013) Universality for the focusing nonlinear schrödinger equation at the gradient catastrophe point: rational breathers and poles of the tritronquée solution to painlevé i. *Communications on Pure and Applied Mathematics* 66(5):678–752.
- <sup>36</sup> Tikan A, et al. (2017) Universality of the peregrine soliton in the focusing dynamics of the cubic nonlinear schrödinger equation. *Physical Review Letters* 119(3):033901.
- <sup>37</sup> Akhmediev N, Ankiewicz A, Taki M (2009) Waves that appear from nowhere and disappear without a trace. *Physics Letters A* 373(6):675–678.
- <sup>38</sup> Shrira VI, Geogjaev VV (2010) What makes the peregrine soliton so special as a prototype of freak waves? *Journal of Engineering Mathematics* 67(1):11–22.
- <sup>39</sup> Akhmediev N, Dudley JM, Solli D, Turitsyn S (2013) Recent progress in investigating optical rogue waves. *Journal of Optics* 15(6):060201.
- <sup>40</sup> Toenger S, et al. (2015) Emergent rogue wave structures and statistics in spontaneous modulation instability. *Scientific reports* 5.
- <sup>41</sup> Chabchoub A (2016) Tracking breather dynamics in irregular sea state conditions. *Physical review letters* 117(14):144103.
- <sup>42</sup> Bailung H, Sharma S, Nakamura Y (2011) Observation of peregrine solitons in a multicomponent plasma with negative ions. *Physical review letters* 107(25):255005.
- <sup>43</sup> Kibler B, et al. (2010) The peregrine soliton in nonlinear fibre optics. *Nature Physics* 6(10):790.
- <sup>44</sup> Suret P, et al. (2016) Single-shot observation of optical rogue waves in integrable turbulence

- using time microscopy. *Nature communications* 7.
- <sup>45</sup> Mohamad MA, Cousins W, Sapsis TP (2016) A probabilistic decomposition-synthesis method for the quantification of rare events due to internal instabilities. *J. Comp. Phys.* 322:288–308.
- <sup>46</sup> Farazmand M, Sapsis TP (2017) A variational approach to probing extreme events in turbulent dynamical systems. *arXiv preprint arXiv:1704.04116*.
- <sup>47</sup> Farazmand M, Sapsis TP (2017) Reduced-order prediction of rogue waves in two-dimensional deep-water waves. *Journal of Computational Physics* 340:418–434.
- <sup>48</sup> Cox SM, Matthews PC (2002) Exponential time differencing for stiff systems. *J. Comp. Phys.* 176(2):430–455.
- <sup>49</sup> Kassam AK, Trefethen LN (2005) Fourth-order time-stepping for stiff pdes. *SIAM J. Sci. Comput.* 26(4):1214–1233.
- <sup>50</sup> Borzi A, Schulz V (2011) *Computational optimization of systems governed by partial differential equations*. (SIAM).